Bulk and Surface Chemistry of the Niobium MAX and MXene Phases from Multinuclear Solid-State NMR Spectroscopy

Kent J. Griffith,[1,2,†] Michael A. Hope,[1,†] Philip J. Reeves,[1] Mark Anayee,[3] Yury Gogotsi,[3]

Clare P. Grey[1]

[1]Department of Chemistry, University of Cambridge, Cambridge, CB2 1EW, United Kingdom
[2]Department of Chemistry and Department of Materials Science and Engineering, Northwestern University, Evanston, IL 60208, United States
[3]A. J. Drexel Nanomaterials Institute, and Department of Materials Science and Engineering, Drexel University, Philadelphia, PA 19104, United States
[†]Authors contributed equally

Abstract

MXenes, derived from layered MAX phases, are a class of two-dimensional materials with emerging applications in energy storage, electronics, catalysis, and other fields due to their high surface areas, metallic conductivity, biocompatibility and attractive optoelectronic properties. MXene properties are heavily influenced by their surface chemistry, but a detailed understanding of the surface functionalization is still lacking. Solid-state nuclear magnetic resonance (NMR) spectroscopy is sensitive to the interfacial chemistry, the phase purity including the presence of amorphous/nanocrystalline phases, and the electronic properties of the MXene and MAX phases. In this work, we systematically study the chemistry of Nb MAX and MXene phases, Nb_2CT_x and $Nb_4C_3T_x$, with their unique electronic and mechanical properties, using solid-state NMR spectroscopy and examine a variety of nuclei (^1H, ^{13}C, ^{19}F, ^{27}Al and ^{93}Nb) with a range of one- and two-dimensional correlation, wideline, high-sensitivity, high-resolution, and/or relaxation-filtered experiments. Hydroxide and fluoride terminations are identified, found to be intimately mixed, and their chemical shifts are compared with other MXenes. This multinuclear NMR study demonstrates that diffraction alone is insufficient to characterize the phase composition of MAX and MXene samples as numerous amorphous or

nanocrystalline phases are identified including NbC, AlO_6 species, aluminum nitride or oxycarbide, $AlF_3 \cdot n H_2O$, Nb metal, and unreacted MAX phase. To the best of our knowledge, this is the first study to examine the transition-metal resonances directly in MXene samples, and the first ^{93}Nb NMR of any MAX phase. The insights from this work are employed to enable the previously-elusive assignment of the complex overlapping $^{47/49}$Ti NMR spectrum of Ti_3AlC_2. The results and methodology presented here provide fundamental insights on MAX and MXene phases and can be used to obtain a more complete picture of MAX and MXene chemistry, to prepare realistic structure models for computational screening, and to guide the analysis of property measurements.
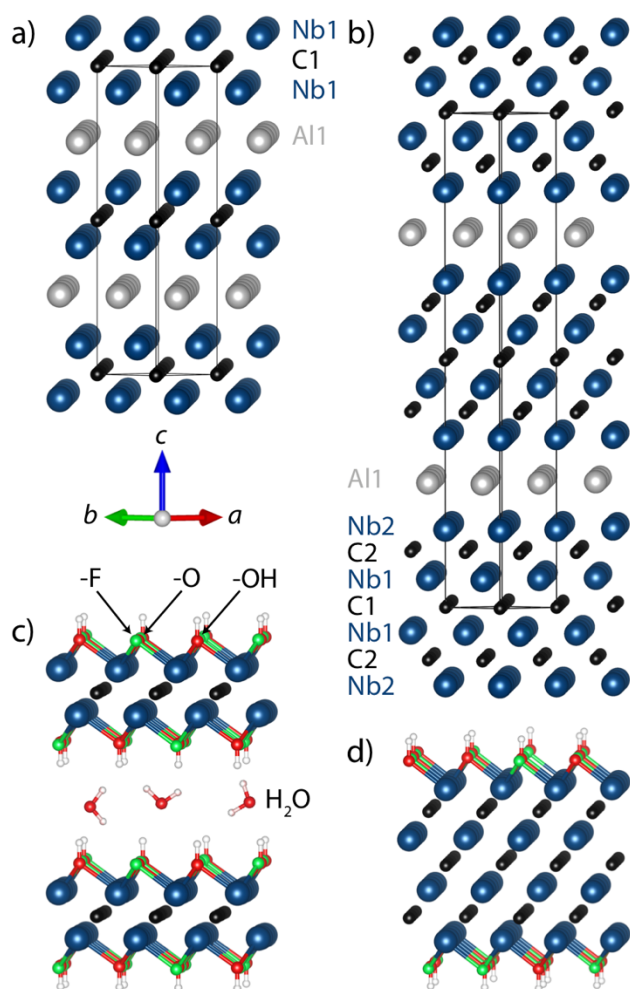
Introduction

Figure 1 – Crystal structures of the niobium MAX and surface-terminated MXene compounds. In a) Nb_2AlC and b) Nb_4AlC_3, the crystallographic sites are labeled and the unit cells are outlined. Table 1 describes the local coordination around each atom. The corresponding MXenes c) Nb_2CT_x and d) $Nb_4C_3T_x$, showing –F, –O and –OH terminations; two layers and interlayer water are shown for Nb_2CT_x.

MAX phases (M = early transition metal; A = Al, Si, Ga; X = C, N) are a large class of 3D layered ternary compounds with the stoichiometry $M_{n+1}AX_n$ ($1 \leq n \leq 3$).[1–4] MXenes are a similarly diverse class of 2D compounds derived from MAX phases via etching of the A-site atoms.[5] It is well-established that MXenes are surface-terminated, and thus better represented by the formula $M_{n+1}X_nT_x$ (T = termination), however the nature of the surface composition, coordination, and spatial arrangements are exceptionally challenging to ascertain (Figure 1). Both material families have extremely diverse applications: MAX phases are used for industrial components such as heating elements and gas burner nozzles with high temperature applications[1,3,6] and MXenes are being tested as functional materials for applications in energy storage,[7,8] hydrogen[9,10] and oxygen[11,12] evolution catalysis, cancer therapeutics,[13] electromagnetic interference shielding,[14,15] and wireless communication[16]. The electronic and functional properties of MXenes depend strongly on the surface terminations,[17–20] so a deeper understanding of the surface chemistry is required to optimize the performance in these applications.

As the first reported MXene, $Ti_3C_2T_x$ has been the most thoroughly studied member of this family, while many other MXenes have been, and continue to be, synthesized and applied to diverse functions. In this work, on the other hand, we focus on the less studied $4d$ transition metal-based niobium MAX and MXene phases including Nb_4AlC_3, $Nb_4C_3T_x$, Nb_2AlC, and Nb_2CT_x, and Nb_2SnC. While Nb_2AlC[21] and Nb_2SnC[22] were reported in the 1960s, it was not until the 2000s that Nb_4AlC_3 emerged[23] via a synthesis strategy borrowed from the synthesis of the Ta MAX series. The syntheses of Nb_2CT_x[24] and $Nb_4C_3T_x$[25] MXenes were then reported in 2013 and 2014, respectively, by selective etching of Al from Nb_2AlC and Nb_4AlC_3, following the same methodology as for $Ti_3C_2T_x$. Neither the intermediate compound Nb_3AlC_2 nor its MXene derivative have been reported; density functional theory (DFT) calculations suggest that this 312 MAX phase is dynamically unstable.[26] The Nb MAX and MXene phases have various interesting properties and potential applications: Nb_2CT_x[24,27] and $Nb_4C_3T_x$[28,29] have attracted recent interest as lithium-ion battery anodes, $Nb_4C_3T_x$ is one of the most conductive and strongest MXene phases,[25] which makes it promising for field-effect transistors and mechanical applications,[30] and Nb_2SnC[31] and Nb_2AlC[32] are superconducting up to 7.8 K and 0.440 K, respectively. Superconductivity was recently observed in Nb_2CT_x at 4.5 to 7.1 K, the temperature depending on the surface termination.[33]

The structures of the Nb MAX and MXene phases are shown in Figure 1, with the first-shell coordination numbers and geometry given in Table 1. Nb_4AlC_3 and $Nb_4C_3T_x$ contain two distinct crystallographic Nb sites and two C sites. Nb2 and C2 are the sites nearer to the Al/etched layer and will thus be referred to as 'external' while Nb1 and C1 are denoted 'internal' following the assignments in ICSD crystal structure files 160755[23] and 606236[21]. Nb_2AlC and Nb_2CT_x contain one Nb site and one C site; these are necessarily 'external'. Both MAX phases contain a single Al environment with trigonal prismatic coordination to six

niobium atoms. Note that the MXene coordination in Table 1 is described in the absence of termination groups (T).

Table 1 – Local atomic sites in Nb MAX and MXene phases.

Compound	Coordination by Crystallographic Site				
	Nb1	Nb2	Al	C1	C2
Nb_2AlC	*fac*-$NbAl_3C_3$ (D)	–	$AlNb_6$ (P)	CNb_6 (R)	–
Nb_4AlC_3	NbC_6 (R)	*fac*-$NbAl_3C_3$ (D)	$AlNb_6$ (P)	CNb_6 (R)	CNb_6 (R)
Nb_2C	NbC_3 (T)	–	–	CNb_6 (R)	–
Nb_4C_3	NbC_3 (T)	NbC_3 (T)	–	CNb_6 (R)	CNb_6 (R)

D = distorted octahedron; R = regular octahedron; T = trigonal pyramid; P = prismatic.

Solid-state NMR spectroscopy is a versatile toolkit that is sensitive to bonding and electronic properties with the ability to probe different elements individually. Additionally, there is no requirement for long-range periodic order in NMR, therefore, it can be readily applied to defect and surface chemistry as well as to nanoparticles. In particular, NMR can reveal the presence of amorphous impurities which are invisible to diffraction techniques. All the elements in the niobium aluminum carbide phases are NMR active and relatively accessible: ^{13}C is I = ½ with a natural abundance of 1.1%, while ^{93}Nb (I = 9/2) and ^{27}Al (I = 5/2) are 100% naturally abundant quadrupolar nuclei. The quadrupolar nature of the latter two nuclei means that they are extremely sensitive to the symmetry of their local environment. Despite the analytical utility, NMR investigations of MAX and MXene phases are sparse. Lue *et al.* measured static ^{27}Al NMR spectra of the 3*d* transition metal MAX series Ti_2AlC, V_2AlC, and Cr_2AlC,[34] finding relatively long nuclear relaxation times and systematically decreasing nuclear quadrupole coupling constants and Knight shifts from Ti toward Cr.[34] The first NMR study of a MXene was by Harris *et al.* who identified –OH and –F surface terminations in V_2C by ^{1}H and ^{19}F NMR spectroscopy and demonstrated the proximity of ^{1}H nuclei to the MXene surfaces by using ^{1}H→^{13}C cross polarization (CP).[35] Hope *et al.* later quantified the concentrations of –OH and –F terminations on Ti_3C_2 MXene, which were found to be highly dependent on the synthesis method, and showed the terminations to be intimately mixed using ^{1}H–^{19}F NMR

correlation experiments.[36] These observations have been extended to further $Ti_3C_2T_x$ syntheses and preparation conditions in a pair of very recent reports.[37,38]

In this work, a comprehensive multinuclear NMR study (^{93}Nb, ^{27}Al, ^{13}C, ^{1}H, and ^{19}F) of the bulk structures and surface chemistry of the known $Nb_{n+1}AlC_n$ MAX and $Nb_{n+1}C_nT_x$ MXene phases is performed with a range of one- and two-dimensional techniques,[39] with additional comparisons to Nb_2SnC and the $^{47/49}Ti$ NMR of Ti_3AlC_2 MAX phase. These experiments are supported by DFT-based electronic structure calculations of the electric field gradient (EFG) at the nucleus. The quadrupolar parameters determined by high-resolution magic-angle spinning (MAS) and static wideline ^{93}Nb and ^{27}Al spectra give insights on the local structures of the MAX phases, while ^{93}Nb and ^{13}C spectra reveal the nature of the etching to the corresponding MXene phases, with the ^{93}Nb NMR further confirming that the latter are surface terminated. ^{1}H, ^{19}F and ^{93}Nb two-dimensional NMR spectroscopy then identifies the chemistry and connectivity of the MXene surface terminations. Finally, the presence of diffraction-silent side-products is confirmed, including the observation of aluminum oxides via the ^{27}Al NMR spectra. Overall, these results have important implications for the synthesis, characterization, and functional properties of Nb MAX and MXene phases.

Experimental

Synthesis. Nb_2AlC MAX phase was prepared as described per Naguib et al.[24] Elemental powders of niobium (99.9% metals basis, 325 mesh), aluminum (99.8% purity, 300 mesh), and carbon black (99% purity, 300 mesh) were mixed in a plastic jar with a ratio of 2:1.1:1 Nb:Al:C and ball milled. The powder was placed into an alumina boat and heated under Ar flow to 1600 °C, with a ramp rate of 4 °C·min^{-1}, and sintered for 4 h. After natural cooling to room temperature, the MAX phase was milled into powder and sieved through a 400-mesh sieve.

To prepare Nb_2CT_x MXene, 1.0 g of Nb_2AlC powder was transferred into 20 mL of HF (aqueous, 49%, Millipore-Sigma) over 60 s and stirred for 48 h at 50 °C. The mixture was washed several times by centrifugation at 3500 rpm (5 min/cycle), the supernatant was decanted, and deionized (DI) water was added until the supernatant reached a pH >6. Multilayered MXene powder was collected by filtration through a cellulose acetate membrane (0.45 μm pore size). The delamination of Nb_2CT_x was carried out by transferring 1.0 g of MXene powder into 10 mL of a diluted tetramethylammonium hydroxide (TMAOH) solution (25% in H_2O, Millipore-Sigma). The solution was stirred overnight (~18 h) at room temperature. To remove excess TMAOH, the mixture was washed by centrifugation with DI water (50 mL) at 3500 rpm for 20 min followed by decantation of the supernatant. The process was repeated until the supernatant reached a pH <8. Then, the sediment was dispersed in 50 mL of deionized water and sonicated for 1 h in an ice-bath with Ar bubbling. Finally, the mixture was centrifuged for 1 h at 3500 rpm, and the supernatant was carefully removed to leave the MXene sediment in the bottom of the tube.

To prepare Nb_4AlC_3, powders of niobium (99.9% metals basis, 325 mesh), aluminum (99.8% purity, 300 mesh), and carbon black (99% purity, 300 mesh) were mixed and the synthesis was performed as previously reported.[28] To prepare $Nb_4C_3T_x$, 0.4 g Nb_4AlC_3 powder was added to 30 mL HF solution (aqueous, 49%, Millipore-Sigma) and stirred at room temperature (20–25 °C) for 6 days. The produced acidic mixture was washed by DI water followed by centrifugation (3500 rpm, 2 min per cycle). After each centrifugation cycle, the supernatant was discarded and the sediment was dispersed in DI water until neutral pH (~7) was reached. In order to delaminate the $Nb_4C_3T_x$, 1 mL of TMAOH (25% in H_2O, Millipore-Sigma) was mixed with 9 mL DI H_2O, added to $Nb_4C_3T_x$, and shaken for 15 minutes at room temperature. The excess TMAOH was separated from the product by repeated centrifugation at 3500 rpm.

Diffraction. X-ray diffraction (XRD) patterns were recorded in reflection mode under sample rotation on a PANalytical Empyrean diffractometer with a Cu Kα (1.540598 Å + 1.544426 Å) X-ray source.

Solid-state NMR Spectroscopy. ^{1}H, ^{13}C and ^{19}F spectra were recorded at 11.75 T. ^{1}H and ^{19}F spectra were recorded with a Hahn echo pulse sequence, or by taking the isotropic slice of a magic angle turning, phase adjusted spinning sideband (MATPASS) sideband-separation experiment.[40] ^{1}H and ^{19}F experiments were performed at 50 kHz MAS in a 1.3 mm HX probe with recycle delays of 15 s and 0.3 s, respectively. ^{13}C spectra were recorded in a 2.5 mm HX probe at 25 kHz MAS, with a 1 s recycle delay and a Hahn echo pulse sequence; the MAX samples were diluted with 20 wt% boron nitride to facilitate spinning (of these metallic samples). ^{1}H/^{93}Nb and ^{19}F/^{93}Nb TRAPDOR experiments were performed at 25 kHz with a 2.5 mm HX probe and a recycle delay of 1 s. ^{1}H/^{19}F HECTOR experiments were performed at 20 kHz with a 2.5 mm HX probe with recycle delays of 1 s or 3 s. ^{27}Al and ^{93}Nb spectra were recorded at 16.4 T with a 1.3 mm or 4.0 mm HXY probe under static or MAS conditions with a single pulse or a Hahn echo pulse sequence and a recycle delay of 0.3–100 s for ^{27}Al and 0.1–0.5 s for ^{93}Nb, as described in each figure. Broad static ^{93}Nb spectra were collected with the assistance of an external automatic tuning/matching (eATM) robot[41]. These variable-offset cumulative spectra (VOCS) measurements were recorded in steps of 170 kHz (~1000 ppm). ^{47,49}Ti spectra were recorded with a CPMG pulse sequence using VOCS acquisition in steps of 80 kHz (~2000 ppm) with 115 echoes of 0.8 ms each and recycle delays of 0.1 s; the sub-spectra were combined by taking the skyline projection:[42] for each point, the highest intensity value from the overlapping sub-spectra is taken, rather than adding their intensities together. ^{1}H spectra were referenced to adamantane at 1.81 ppm, ^{13}C spectra to the tertiary carbon of adamantane at 38.5 ppm, ^{19}F spectra to LiF at −203 ppm, ^{27}Al spectra to AlF$_3$ at −15 ppm, ^{93}Nb spectra to LiNbO$_3$ at −1004 ppm[43], and ^{47,49}Ti spectra to the ^{49}Ti signal of SrTiO$_3$ at −843 ppm.

The isotropic shift δ_{iso} is defined in the Haeberlen convention $\delta_{iso} = \frac{\delta_{XX} + \delta_{YY} + \delta_{ZZ}}{3}$ with the chemical shift anisotropy (CSA) defined as $CSA = \delta_{ZZ} - \delta_{iso}$ and the shift asymmetry η_{CSA} defined as $\eta_{CSA} = \frac{\delta_{YY} - \delta_{XX}}{\delta_{ZZ} - \delta_{iso}}$. With these definitions, the principal components of the shift tensor are ordered such that $|\delta_{ZZ} - \delta_{iso}| \geq |\delta_{XX} - \delta_{iso}| \geq |\delta_{YY} - \delta_{iso}|$. $N.b.$ This definition of CSA is sometimes referred to as the reduced anisotropy, which is equal to 2/3 of the 'full' anisotropy $\delta_{ZZ} - \frac{\delta_{XX} + \delta_{YY}}{2}$ used by some authors and programs. The quadrupolar coupling constant, C_Q, is defined by the nuclear quadrupole moment Q ($Q_{\text{Nb-93}} = 32(2)$ fm^2; $Q_{\text{Al-27}} = 14.66(10)$ fm^2)[44] and the largest principal component V_{ZZ} of the EFG at the nucleus according to $C_Q = \frac{eQV_{ZZ}}{h}$ where e is the electric charge and h is Planck's constant. The quadrupolar asymmetry parameter η_Q is also defined by the EFG tensor components as $\eta_Q = \frac{V_{XX} - V_{YY}}{V_{ZZ}}$ ordered such that $|V_{ZZ}| \geq |V_{YY}| \geq |V_{XX}|$.

Calculations. Density functional theory (DFT) calculations were performed with the CASTEP planewave pseudopotential code.[36] The calculations used the Perdew–Burke–Ernzerhof (PBE) exchange–correlation functional[37] and Vanderbilt ultrasoft pseudopotentials.[38] MAX crystal structures from the Inorganic Crystal Structure Database were used as starting models (ICSD606236 for Nb$_2$AlC and ICSD160755 for Nb$_4$AlC$_3$). Prior to the EFG calculations, atomic positions were optimized (with lattice parameters held constant) until the force on any atom was smaller than 10 meV·Å^{-1}. All calculations used a planewave energy cut-off energy of 600 eV and a Monkhorst–Pack[39] grid with a spacing finer than $2\pi \times 0.04$ Å^{-1} to sample the Brillouin zone. Computed EFG parameters were used as the starting point to fit the experimental ^{27}Al and ^{93}Nb spectra.

Results and Discussion

MAX bulk structure characterization. XRD analysis of the Nb$_2$AlC sample (Figure S1) showed Nb$_4$AlC$_3$ as a minor (~5% from Rietveld refinement) secondary phase. No additional

peaks were visible beyond those of the two MAX phases. The Nb_4AlC_3 diffraction pattern showed a NbC-like impurity (~8%) and a small, broad unindexed peak just above the background signal at 26.7°; no Nb_2AlC was detected in the Nb_4AlC_3 sample.
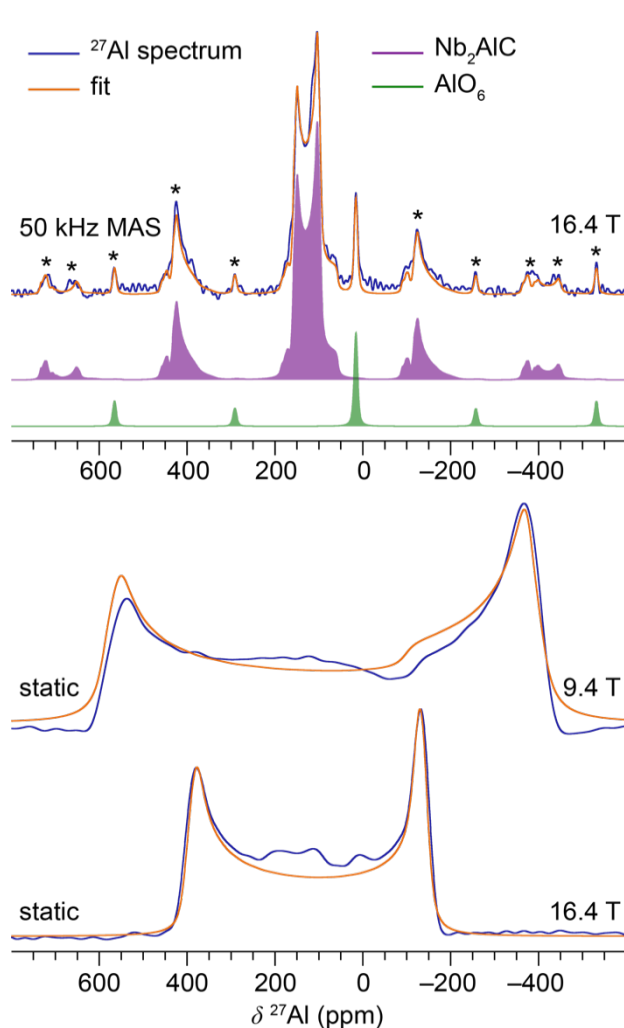

Figure 2 – ^{27}Al NMR spectra of Nb_2AlC at 50 kHz MAS (top) and static (bottom). MAS rate and magnetic field are given for each spectrum. The recycle delays were 100 s and 0.35 s for the MAS and static spectra, respectively. The static spectra were T_1-filtered to facilitate efficient recording of the fast-relaxing MAX signal whereas the MAS spectrum was recorded under quantitative conditions to observe all aluminum environments. Spinning sidebands are denoted with asterisks. See Table 2 for fitting parameters.
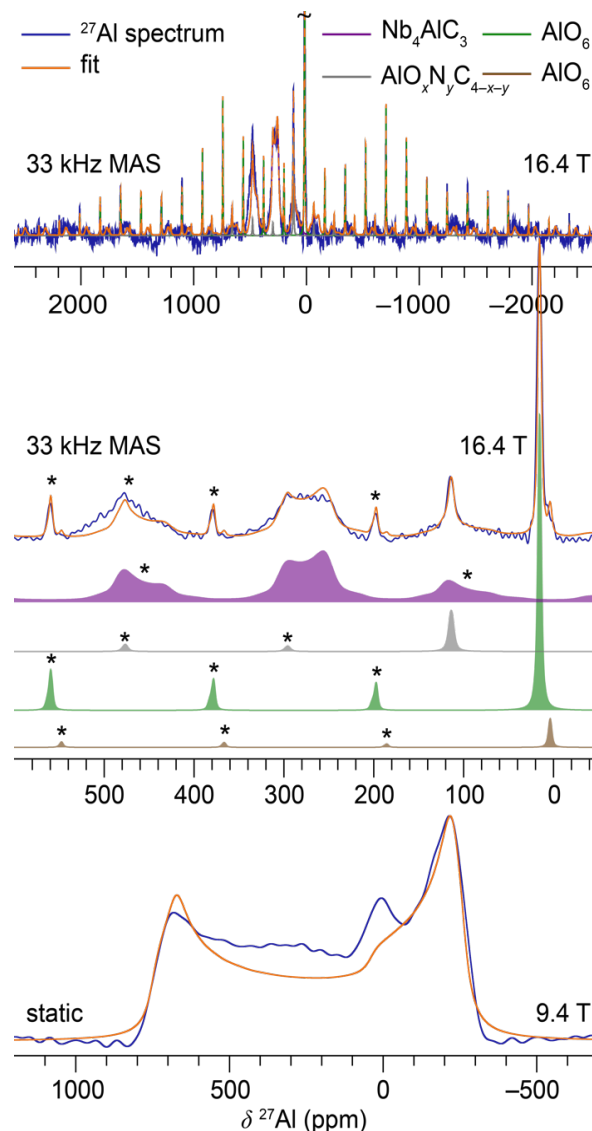
Figure 3 – ^{27}Al NMR spectra of Nb_4AlC_3 at 33 kHz MAS (top, middle) and static (bottom). Note the different x-axis scales. MAS rate and magnetic field are given for each spectrum. The recycle delays were 90 s and 0.05 s for the MAS and static spectra, respectively. Spinning sidebands are denoted with asterisks. See Table 2 for fitting parameters. The missing intensity in the fit of the static spectrum is ascribed to the AlO_6 environment at ~16 ppm.

^{27}Al NMR spectra of the MAX phases Nb_2AlC and Nb_4AlC_3 are given in Figures 2 and 3, respectively. For each compound, a simultaneous fit was performed over the static and MAS

spectra (Table 2). The DFT calculated quadrupolar parameters served as useful starting points to guide the fits (Table 2). Static spectra were sensitive to the value of the CSA while MAS removed CSA broadening and resulted in spectra that were more sensitive to the isotropic shift and quadrupolar tensor. The positions of discontinuities in the powder lineshape from satellite transitions, where observed, were also used to determine the quadrupolar parameters. The calculated quadrupolar coupling constants matched the experimental values to within <5%.

In addition to aluminum in the MAX phases, ^{27}Al NMR revealed the presence of secondary phases. At short recycle delays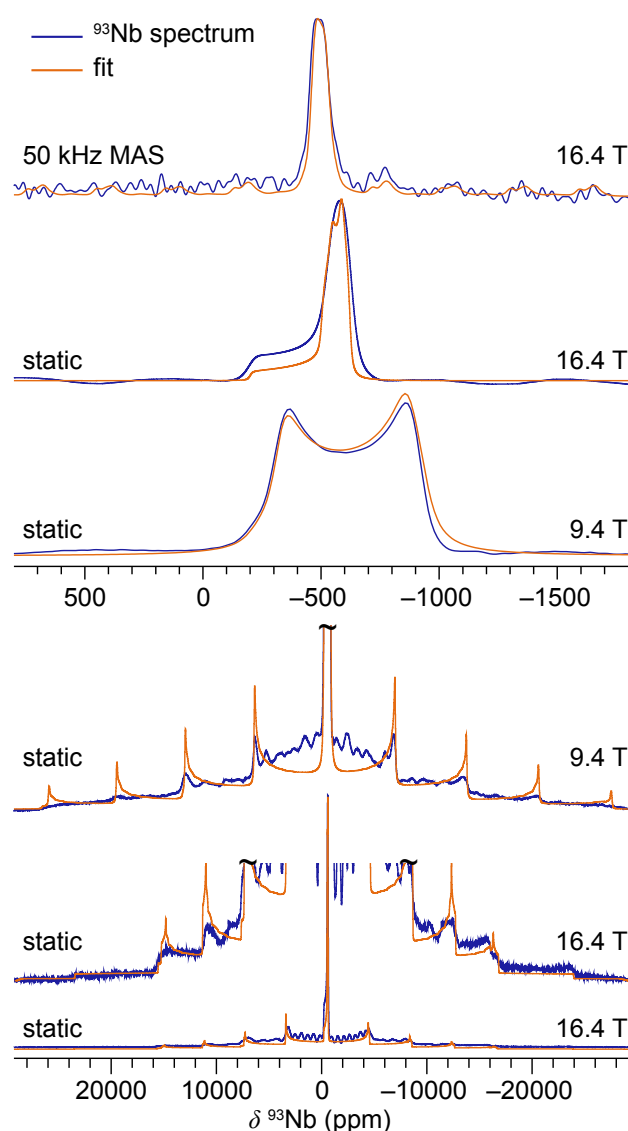, the MAX phases, with fast spin-lattice, T_1, nuclear relaxation from conduction electrons, appear relatively pure (Figure S2–3). However, at longer free induction decay (FID) intervals, the relative intensities of the impurities increase; an indication that the impurities are diamagnetic with longer T_1 relaxation times. The Nb$_2$AlC sample exhibits an unexpected resonance at 16 ppm while the Nb$_4$AlC$_3$ sample shows three additional ^{27}Al resonances at ca. 5, 17, and 115 ppm. The largest impurity in both samples is ascribed to octahedral AlO$_6$ environments as found in corundum alumina,[45] on the basis of the shift (16–17 ppm), C_Q (ca. 2.4 MHz, upper limit ≤4 MHz) and T_1 relaxation time (18 s). The Nb$_4$AlC$_3$ sample signal at 5 ppm is also

Figure 4 – ^{93}Nb NMR spectra of Nb$_2$AlC. MAS rate and magnetic field are given for each spectrum. See Table 2 for fitting parameters.

consistent with octahedral AlO_6, as found in e.g. boehmite, gibbsite, or γ-alumina.[46] The oxide environments could arise from secondary oxide phases, or from the oxide layers previously observed by XPS to form on the surface of MAX particles.[47] The resonance at 115 ppm appears at a higher frequency than for typical aluminum oxides or fluorides[48]; it does coincide with the shift range of aluminum carbide Al_4C_3 (111–120 ppm) but the maximum C_Q value for the observed resonance is ca. 4.5 MHz while Al_4C_3 has two Al sites with C_Q magnitudes of 14–17 MHz.[49,50] Hayes et al. identified aluminum oxycarbide impurities with smaller C_Qs in their recent study of commercial Al_4C_3 so a related aluminum species is plausible here.[50] Another possibility is the tetrahedral aluminum nitride environment that appears at around 110–115 ppm in AlN and in aluminum oxynitrides with a C_Q of a few MHz, consistent with the resonance observed here.[51–54] Note that the ^{27}Al signal from Nb_2AlC covers a range of ~90–170 ppm, so the impurity at 115 ppm is less pronounced but it can be clearly seen as a shoulder that appears as the interval between scans increases (Figure S2). Quantitative spectra recorded with recycle delays of 90–100 s (Figure S2) revealed the relative ratios of the MAX and impurity (or surface) species in the samples from the perspective of aluminum content.[47] For the Nb_2AlC sample, a ratio of 89:9:2 was found for the MAX signal at 169 ppm and the impurity resonances at 16 and 115 ppm, respectively. For the Nb_4AlC_3 sample, a ratio of 56:34:7:3 was found for the MAX signal at 319 ppm and the impurity resonances at 17, 5, and 115 ppm, respectively.

Table 2 – Experimental (shift and quadrupolar) and calculated (quadrupolar only) NMR parameters of Nb_2AlC and Nb_4AlC_3.[a]

Phase	Site	δ_{iso} (ppm)	CSA	η_{CSA}	C_Q (MHz)		η_Q		Euler angles β (°)[c]
					Exp.	Calc.[b]	Exp.	Calc.	
	Nb1	−475(10)[d]	280(50)	0.1(1)	32.3(3)	−30.8	0.01(1)	0.00	5(2)
Nb_2AlC	Al1	171(2)	−275(20)	0.2(1)	15.7(2)	−16.0	0.05(5)	0.00	2(5)
	C1	293(1)	n/d	n/d					
Nb_4AlC_3	Nb1	−1700(5)	300(200)	0.0(1)	2(1)	2.5	n/d	0.00	n/d
	Nb2	−840(20)	650(200)	0.0(1)	32(5)	−33.5	0.00(5)	0.00	80(10)

Al1	319(2)	–280(10)	0.4(2)	15.6(2)	–16.0	0.10(10)	0.00	0(5)
C1	238(2)	n/d	n/d					
C2	324(2)	n/d	n/d					

[a] Static and magic angle spinning spectra (in some cases at multiple fields) were fit to a single model. Estimated errors in the last digit are given in parentheses, derived from lineshape fitting.

[b] The sign of the quadrupolar coupling can be calculated but is not determined experimentally from the spectrum of a polycrystalline sample.

[c] The fits are only sensitive to the β angle because η is nearly zero.

[d] The isotropic shift is temperature-dependent and thus varies with MAS rate. The static ^{93}Nb spectrum of Nb_2AlC was fit with –475(10) ppm while the 50 kHz spectrum was fit with –445(5) ppm.

n/d = not determined, either due to insufficient signal-to-noise (^{13}C) or because the fit was insensitive to this parameter.

Cells corresponding to the quadrupolar properties are left blank for ^{13}C because it is a $I = \frac{1}{2}$ nucleus.

Quadrupolar ^{93}Nb NMR spectra of the compounds were recorded under MAS and static conditions. A fit of the ^{93}Nb NMR data of Nb_2AlC reproduced the central and satellite transitions of the spectrum (Figure 4, Table 2), with calculated and measured nuclear quadrupolar coupling constants in close agreement. The Hahn echo and quadrupolar Carr–Purcell–Meiboom–Gill (QCPMG) ^{93}Nb MAS spectra of Nb_4AlC_3 (Figure 5) showed a number of overlapping peaks that could not be resolved by variable MAS rates due to their individual linewidths (full-width at half-maximum (FWHM) > 40 kHz) and the static spectrum also showed overlapping lineshapes

Figure 5 – ^{93}Nb MAS NMR spectra of the Nb_4AlC_3 sample (45 kHz MAS, 16.4 T). Several methods were used to study this sample including (a) the isotropic slice of a pjMATPASS experiment; (b) a Hahn echo— deconvoluted in grey with the internal site Nb1 in green, the external site Nb2 orange, and NbC in red; and (c) a QCPMG measurement.

(Figure S4). To overcome this challenge, a MATPASS experiment was performed; the isotropic slice showed three broad, featureless resonances at –840, –1700, and –2340 ppm (Figure 5). However, only two distinct Nb environments are expected in Nb_4AlC_3. The low
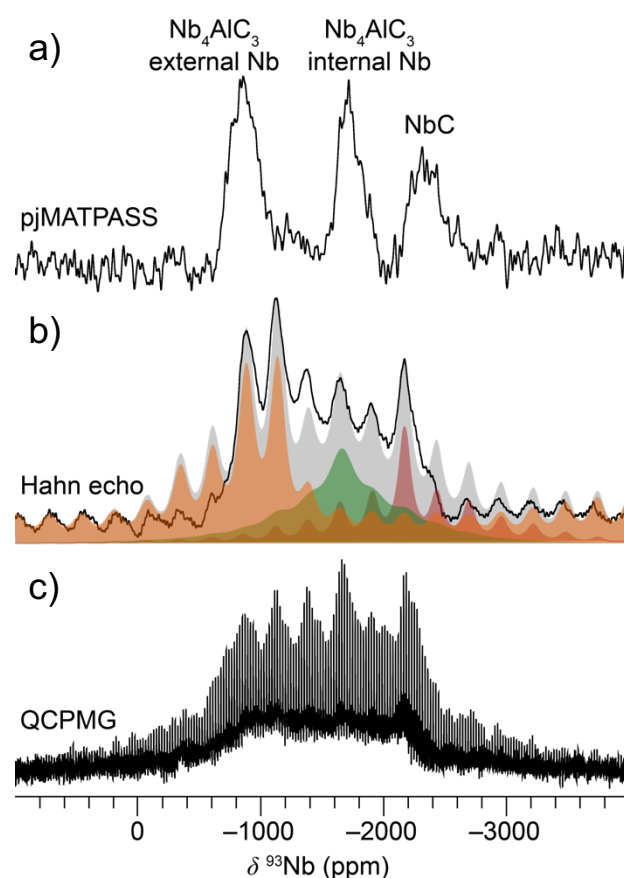
frequency ^{93}Nb resonance matches that of NbC (Figure 5a,b), as do the ^{13}C NMR data (*vide infra*). Stoichiometric NbC should give a sharp ^{93}Nb signal with $C_Q = 0$ due to the cubic site symmetry of the 12-coordinate niobium atom, however nonstoichiometry is common in NbC,[55] depending on the preparation conditions, with NbC_x ($0.7 \leq x < 1$) yielding quadrupolar ^{93}Nb signals.[56,57] Overlapping lines preclude an accurate fitting of the quadrupolar parameters of the NbC_x impurity in Nb_4AlC_3 here but a small C_Q (~2 MHz) improved the fit. For Nb_2SnC (Figure S5), a sharp ^{93}Nb signal was observed with an isotropic shift of $-189(3)$ ppm; this is 300 ppm higher frequency than the isostructural Nb_2AlC. In the wideline static VOCS measurement, Nb metal was also observed as a secondary phase at ~7200 ppm.

The ^{13}C NMR spectrum of Nb_2AlC (Figure 6a, bottom) shows a single resonance at 293 ppm corresponding to the single carbon environment in the 211 phase. The ^{13}C NMR spectrum of Nb_4AlC_3 (Figure 6b, bottom) shows two resonances at 324 ppm and 238 ppm corresponding to the outer (C2) and in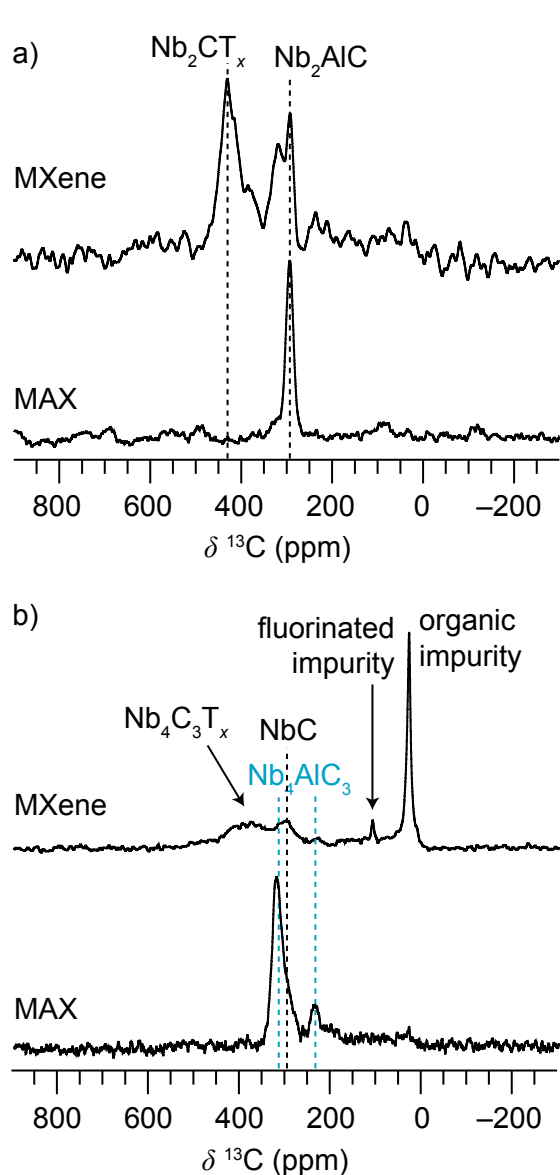ner (C1) carbon sites of Nb_4AlC_3, respectively. For both Nb MAX phases, the large ^{13}C shift is evidence of metallic conduction resulting in a Knight shift; the shifts are larger than observed for V_2AlC (208 ppm),[35] but less than for Ti_3AlC_2 (566 ppm)[36]. There is a significant shoulder for the 324 ppm peak which is ascribed to NbC, the single carbon site of which resonates at ~315 ppm (Figure S6); accounting for this signal, the integrated intensities of the inner and outer carbon sites are in reasonable agreement with the expected 2:1 ratio. The ^{13}C and ^{93}Nb data together clearly show the presence of NbC in Nb_4AlC_3, although it is not observed in the X-ray diffraction pattern (Figure S1) because (i) it is present in nanoparticulate or amorphous form and/or (ii) its identification is obstructed by peak overlap. Note, that phases such as amorphous carbon and low levels of Nb_2O_5 would be difficult to observe via these NMR experiments due to the broad nature of those signals and/or overlap with other signals. The presence of alumina suggests that niobia could also be present, and Sarycheva and Gogotsi

Figure 6 – ^{13}C NMR spectra of (a) Nb_2CT_x MXene and Nb_2AlC MAX phase and (b) $Nb_4C_3T_x$ MXene and Nb_4AlC_3 MAX phase at 25 kHz MAS and 16.4 T. Resonances are labeled, dashed lines are guides to the eye.

observed amorphous carbon and titania in a degraded $Ti_3C_2T_x$ sample via Raman spectroscopy.[58]

MXene bulk structure characterization

By etching out the aluminum, the MAX phases were converted to MXenes. However, the Nb_2CT_x also has a significant amount of unreacted Nb_2AlC, while NbC remains present as an impurity in $Nb_4C_3T_x$, as previously seen for other MAX/MXene samples.[25,59]

The ^{93}Nb NMR spectra of Nb_2CT_x and $Nb_4C_3T_x$ are shown in Figure 7 and Figure S7. Since niobium atoms are located at the outer surface of the 2D MXene sheets, the number of distinct Nb local environments and NMR signals depends on the surface terminations. The ^{93}Nb lineshape of Nb_2CT_x was simulated with two quadrupolar lines, providing a reasonable fit to the data (Figure 7); the minor but sharper signal is consistent with Nb_2AlC, the broader signal was attributed to Nb_2CT_x and was fit with $\delta_{iso} = -790(30)$ ppm, CSA $= -350(50)$ ppm, $\eta_{CSA} = 0.5(3)$, $C_Q = 77(3)$ MHz, $\eta_Q = 0.2(1)$, Euler angles $\alpha,\beta,\gamma = 0°, 50(10)°, 0°$. The C_Q for Nb_2CT_x is more than double that of Nb_2AlC, providing spectral evidence for the reduction of symmetry at the MXene surface. Furthermore, the non-zero η_Q indicates a breaking of the three-fold symmetry of the Nb site at the surface, presumably due to the surface terminations. Calculations for a bare Nb_2C surface predict a ^{93}Nb C_Q of 122 MHz, so the lower observed C_Q is also evidence for the surface terminations which result in a more symmetric charge distribution than a bare surface. Basic ordered models for surface-terminated Nb_2CT_x ($T_x = F_2$, $(OH)_2$, $(OH)F$, O_2, O) give calculated C_Q values ranging from 36–109 MHz (Table S1), which are consistent with the experimental C_Q of 77 MHz. The best agreement is for fluoride and oxide termination, which may suggest a greater proportion of fluoride and oxide terminations than hydroxyl terminations, as previously observed for $Ti_3C_2T_x$.[36] Meanwhile, the ^{93}Nb lineshape of $Nb_4C_3T_x$ is substantially broader. An exact fitting of the lineshape could not be

obtained due to the difficulty of distinguishing a potential distribution of surface terminations, the two Nb sites in $Nb_4C_3T_x$, and the NbC_x impurity, which all overlap. Nevertheless, based on the linewidth a maximum C_Q of ~100 MHz can be determined, ruling out a significant proportion of bare surface (calculated C_Q = 135 MHz for the outer Nb2 site, Table S2). Given
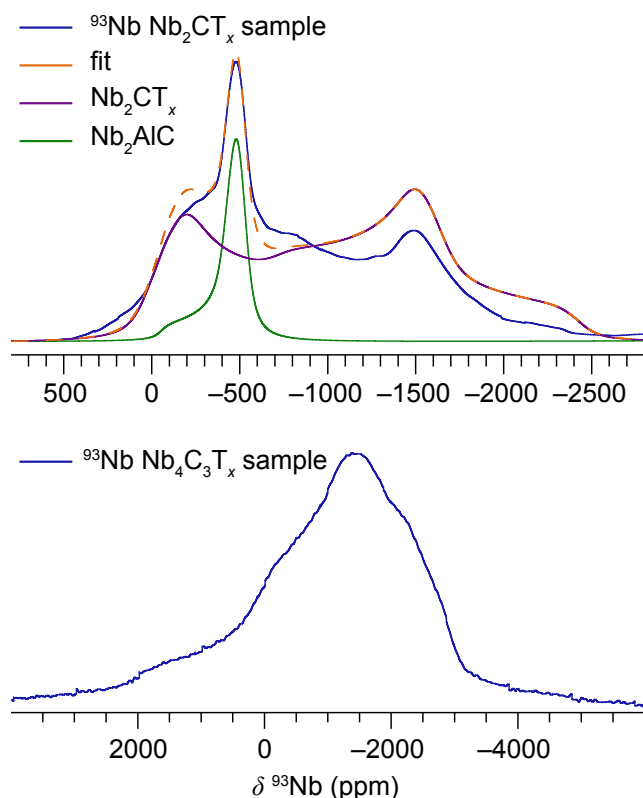

that the calculated quadrupolar parameters for ordered models of surface terminations (Table S2) are in the range 15–70 MHz, chemical shift dispersion and anisotropy of the different Nb environments must make a large contribution to the experimental linewidth.

In the ^{13}C NMR spectra of etched Nb_2AlC, a new signal can be seen at 430 ppm due to Nb_2CT_x MXene, although there is also still unreacted Nb_2AlC present (Figure 6a, top). The intensity in the ^{13}C spectrum between the Nb_2AlC

Figure 7 – Static [93]Nb NMR central transition spectra of the Nb_2CT_x and $Nb_4C_3T_x$ samples at 16.4 T. For Nb_2CT_x, the deconvolution into signals from Nb_2CT_x and Nb_2AlC is shown. For full VOCS spectra, see Figure S7.

and Nb_2CT_x resonances may correspond to partially etched regions with carbon environments intermediate between the MAX and MXene, e.g. regions with a MAX-like aluminum layer on one side, but terminations on the other, or nanoscale clusters of unetched aluminum. After etching Nb_4AlC_3 (Figure 6b, top), a broad high frequency signal can be observed at ~400 ppm, corresponding to $Nb_4C_3T_x$ MXene, although the inner and outer carbon sites cannot be resolved. After etching, the NbC impurity is still evident, as well as signals from other impurities in the sample at 31 and 111 ppm; the former is correlated with a ^{1}H signal at 1 ppm

in the $^1H \rightarrow {}^{13}C$ HETCOR spectrum (Figure S8c), suggesting that this impurity is predominantly alkyl, while the latter can be observed in a $^{19}F \rightarrow {}^{13}C$ cross polarization (CP) experiment (Figure S8b), which, combined with the chemical shift, suggests a $-CF_2-$ moiety in a fluorinated organic species. Notably, the ^{13}C shift increases on etching from the MAX to the MXene for both Nb_2CT_x and $Nb_4C_3T_x$; this is due to an increased Knight shift, corresponding to an increased density of states at the Fermi level for the carbon atoms in the MXene phases. The same increase in ^{13}C shift was observed for V_2CT_x (from 208 ppm to 260 ppm),[35] however, in contrast, the ^{13}C Knight shift actually decreases for $Ti_3C_2T_x$ (from 566 ppm to 380–410 ppm)[36].

As seen from the presence of the Nb_2AlC MAX signal in the ^{93}Nb, ^{27}Al, and ^{13}C spectra, not all aluminum had been etched out during the HF treatment, consistent with prior work on other MXenes: V_2AlC was observed in V_2CT_x samples and Ti_3AlC_2 in $Ti_3C_2T_x$ samples in their respective ^{13}C NMR spectra.[35,36] The ^{27}Al NMR spectra of the MXene samples (Figure S9) also show an AlO_6-like aluminum oxide environment, while the Nb_2CT_x sample also shows a signal consistent with $AlF_3 \cdot nH_2O$, a common impurity in MXenes[60] and one that can be readily identified with NMR spectroscopy.

Since diffraction did not reveal the Al–O, Al–F, or Al–(C,N,O) compounds identified here, these secondary phases must be amorphous, present as small nanoparticles, or hidden under the MAX/MXene diffraction peaks. These findings again highlight that the picture from diffraction alone can be misleading. Furthermore, NbC_x was almost entirely hidden under the Nb_4AlC_3 XRD peaks. A method that is sensitive to amorphous phases such as solid-state NMR and/or quantitative diffraction with an internal standard should be routinely performed to characterize MAX and MXene phases.

Surface terminations of $Nb_4C_3T_x$ and Nb_2CT_x. ^1H and ^{19}F NMR spectra were recorded in order to investigate the surface functionalization of the MXene phases directly. The ^1H NMR

spectrum of Nb_2CT_x as synthesized shows a large signal at 6.3 ppm due to free H_2O as well as two resonances at large chemical shifts of 19.5 and 26.0 ppm (Figure 8a); these latter signals are assigned to –OH surface terminations. –OH terminations were observed in the MXenes V_2CT_x at 85 and 27 ppm[35] and $Ti_3C_2T_x$ between 12.5 and 20 ppm, the exact shift values depending on the synthesis procedure[36,37]. The free H_2O signal can be reduced by drying the MXene at 200 °C *in vacuo* (Figure 8b), after which an additional resonance can be distinguished at 12.2 ppm, as well as sharper signals between −0.5 and 1.6 ppm; the former could be due to a further –OH termination environment, or bound H_2O partaking in strong hydrogen bonding, while the latter are assigned to intercalated volatile contaminants, as was also observed for $Ti_3C_2T_x$. There is also a loss of intensity for the 26.0 ppm signal in particular, which may be due to loss of –OH terminations as H_2O during the drying process.[61]
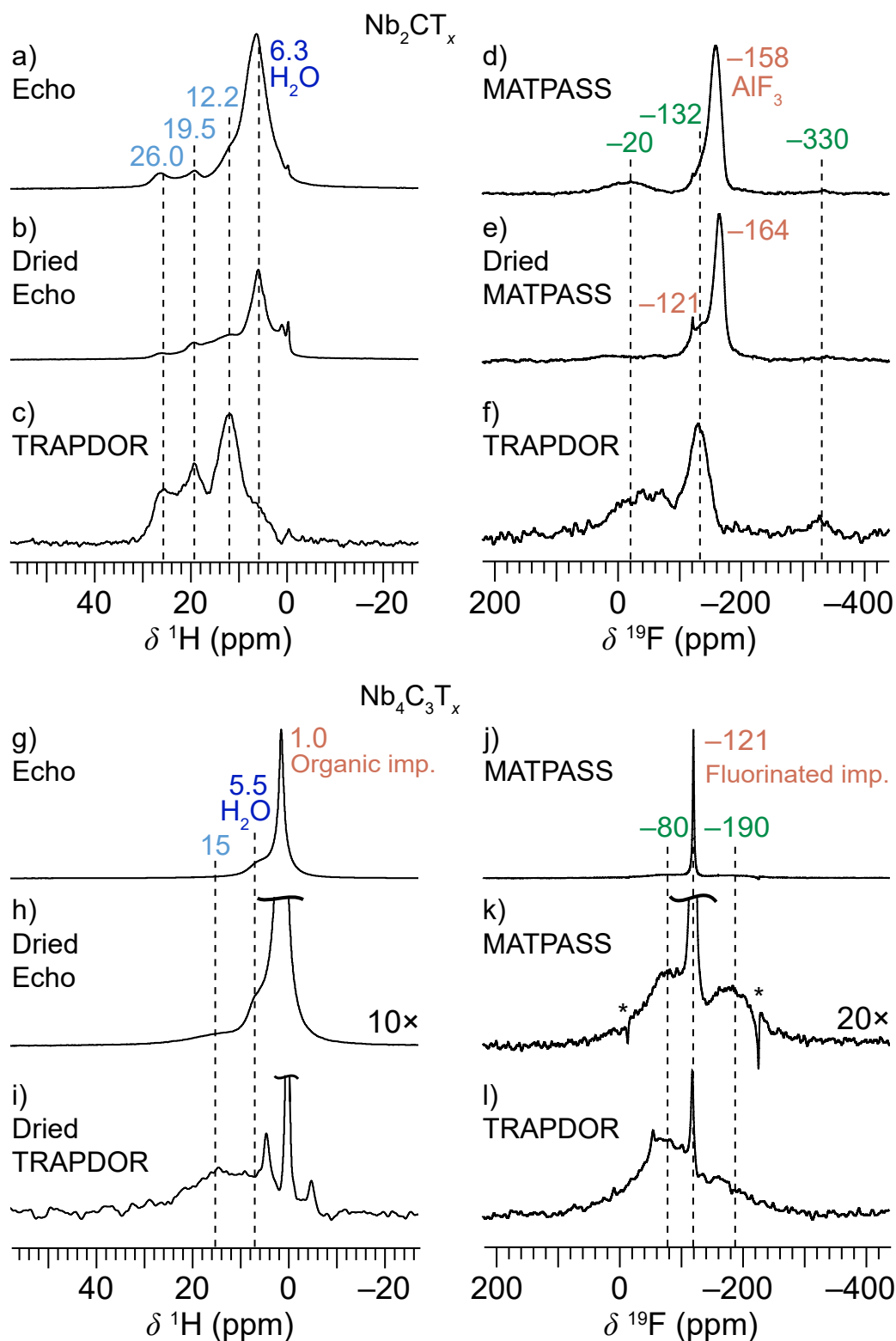
Figure 8 – ^1H and ^{19}F NMR spectra of Nb_2CT_x (a–f) and $Nb_4C_3T_x$ (g–l). The $^1H/^{93}Nb$ and $^{19}F/^{93}Nb$ TRAPDOR difference spectra (c,f,i,l) show ^1H (c,i) or ^{19}F (f,l) atoms near ^{93}Nb atoms. The echo and MATPASS experiments were performed at 50 kHz MAS and the TRAPDOR experiments at 30 kHz, all at a magnetic field strength of 11.7 T. Sidebands are marked with asterisks.

The assignment of the ^{1}H NMR resonances at high chemical shift to surface species on the MXene layers can be confirmed by ^{1}H/^{93}Nb TRAPDOR experiments:[62] for these spectra, a ^{1}H spin echo is recorded with continuous irradiation of ^{93}Nb during only the first half of the echo, thus any dephasing due to recoupled ^{1}H–^{93}Nb interactions is only partially refocused, resulting in a loss of signal intensity for ^{1}H environments in the vicinity of ^{93}Nb; when the difference is taken between spin echoes recorded with and without ^{93}Nb irradiation, these ^{1}H environments (near ^{93}Nb) can be selectively observed. The signals at 12.2, 19.5 and 26.0 ppm can all be clearly observed in the TRAPDOR difference spectra (Figure 8c and Figure S10), confirming their vicinity to Nb atoms at the MXene surface; the signals at less than 5 ppm, on the other hand, are suppressed in the TRAPDOR difference spectra. A weaker TRAPDOR effect is observed for the free H_2O resonance at 6.3 ppm, which suggests that only some of the free H_2O is proximal to Nb and/or that it is mobile; this may be evidence of chemisorbed water, as proposed by Persson et al.[63]

The sideband-separated ^{19}F NMR spectrum of Nb$_2$CT$_x$, recorded with a MATPASS pulse sequence,[40] shows a number of different resonances (Figure 8d). The signal at −158 ppm is due to AlF$_3$·nH$_2$O, a by-product of the etching process also seen in the ^{27}Al spectrum (Figure S8);[36,64] this resonance is suppressed in the ^{19}F/^{93}Nb TRAPDOR difference spectrum (Figure 8f), leaving the signals at −20, −132 and −330 ppm, which must be near Nb. ^{1}H/^{19}F HETCOR experiments (Figure S11) are completely dominated by the H_2O↔AlF$_3$ correlation, so cannot be used to aid assignment of the ^{19}F spectrum. After drying at 200 °C *in vacuo* the AlF$_3$·nH$_2$O resonance shifts to −164 ppm due to changes in hydration, so that the −132 ppm signal can be seen as a shoulder more clearly, and there is also a small, sharp peak at −121 ppm from a fluorinated organic impurity. The ^{19}F signal at −20 ppm is largely removed by drying, so may be tentatively ascribed to –F terminations with strong hydrogen bonding to H_2O molecules, or adjacent –OH terminations (given that the intensity of the –OH signals in the ^{1}H NMR also

decreases on drying). Conversely, the major ^{19}F signal at -132 ppm is assigned to $-$F terminations without strong H bonding. The minor signal at -330 ppm is strongly ionic; it may be a niobium fluoride species formed as a byproduct from excessive etching and could therefore be minimized by using milder etching conditions.[65]

The ^{1}H NMR spectrum of $Nb_4C_3T_x$ (Figure 8g) is dominated by a peak at 1.0 ppm due to the organic impurity identified from the ^{1}H→^{13}C HETCOR experiment (Figure S8c). Further ^{1}H signals at 5.5 ppm and 15 ppm are assigned to H_2O and $-$OH terminations, respectively. Both the organic contaminant and the H_2O signals can be reduced by drying *in vacuo* at 200 °C overnight (Figure 8h), while the $-$OH terminations can be identified in the ^{1}H/^{93}Nb TRAPDOR difference spectrum (Figure 8i and Figure S10). In the TRAPDOR experiment, the 1.0 ppm peak is almost, but not entirely, suppressed; the residual signal and satellite peaks are due to the differential phase (Bloch–Siegert) shift[66,67] introduced by ^{93}Nb irradiation, which results in imperfect cancellation in the difference spectrum.

The ^{19}F MATPASS NMR spectrum for $Nb_4C_3T_x$ is dominated by a resonance at -121 ppm (Figure 8j,k), which is consistent with the fluorinated impurity identified by ^{19}F→^{13}C CP. Two other signals can also be distinguished, centered at ca. -190 and -80 ppm; these are assigned to $-$F terminations as they can clearly be observed in the ^{19}F/^{93}Nb TRAPDOR difference spectrum (Figure 8l), although the sidebands of the terminal $-$F signals are unresolved. Further evidence for the assignment of the $-$OH and $-$F terminations can be seen in the ^{1}H/^{19}F HETCOR spectra: in the ^{19}F→^{1}H spectrum (Figure 9b) a broad correlation is observed between both the H_2O (6.0 ppm) and $-$OH (15 ppm) ^{1}H resonances and ^{19}F intensity between ca. 50 and -300 ppm that corresponds to the signals from $-$F terminations at -190 and -80 ppm, with unresolved spinning sidebands. This supports the assignments of the ^{1}H and ^{19}F spectra, as well as showing that the terminations are intimately mixed, rather than being

segregated into different regions, as also found for $Ti_3C_2T_x$.[36] In contrast, the $^1H \rightarrow {}^{19}F$ spectrum
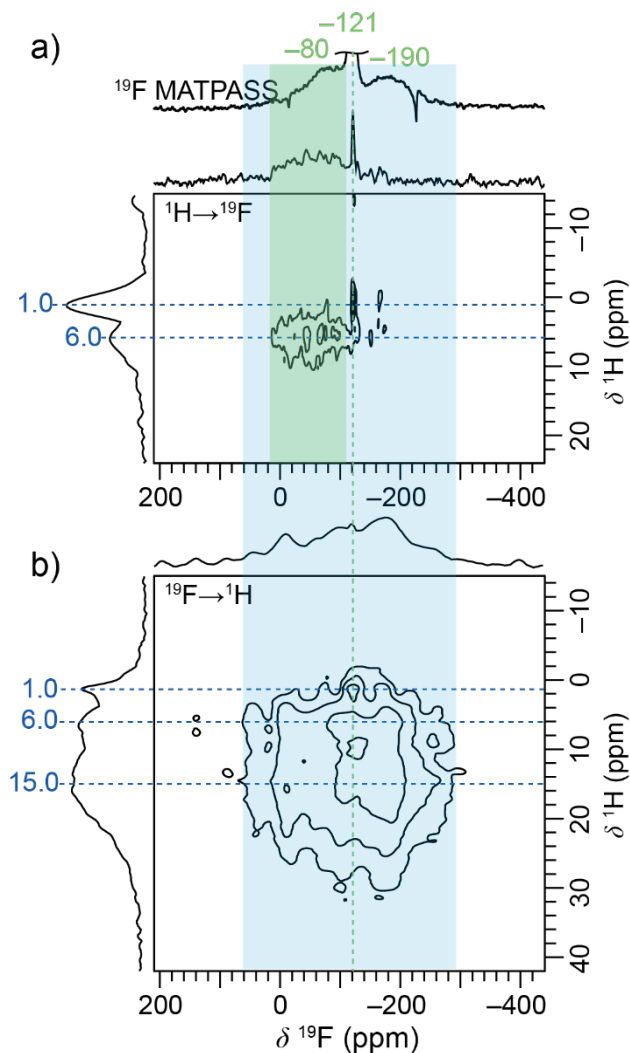

Figure 9: $^1H/{}^{19}F$ HETCOR spectra of $Nb_4C_3T_x$ recorded at 11.7 T and 20 kHz MAS with a 2 ms contact time. The recycle delays were 3 s and 1 s respectively for a) and b). The ^{19}F MATPASS spectrum is shown for comparison. Note that the axes for b) have been swapped relative to convention to allow comparison of the ^{19}F axis.

(Figure 9a) only shows correlation between the ^1H H_2O (6.0 ppm) signal and the −80 ppm –F termination ^{19}F signal. The lack of signal from the –OH terminations is ascribed to a short ^1H $T_{1\rho}$ for this resonance, so that the transverse magnetization decays before developing significant cross polarization. The fact that the H_2O resonance correlates only with the −80 ppm ^{19}F signal suggests that these –F termination environments are associated with interlayer water via hydrogen bonding, whereas those at −190 ppm are not. The higher frequency ^{19}F shift observed for H-bonded –F terminations in $Nb_4C_3T_x$ is also consistent with the assignment of the −20 ppm ^{19}F signal in Nb_2CT_x to strongly H-bonded –F terminations.

Table 3 shows a comparison of the shifts of the observed surface species for the different MXenes studied by ^1H and ^{19}F NMR to date. For the –OH terminations, V_2CT_x is the exception with an extremely large shift of 85 ppm; this is due to a metallic Knight shift, as confirmed by the short T_1 relaxation of this signal,[35] Interestingly, the –F terminations of V_2CT_x do not appear to be significantly Knight shifted and are observed at a similar frequency to those

of $Ti_3C_2T_x$. The –OH ^{1}H shifts obtained for $Ti_3C_2T_x$ have been shown by both Hope et al.[36] and Anayee et al.[37] to depend on the synthesis procedure, but in both cases fall in the range 12.5–20 ppm. In contrast, Kobayashi et al.[38] observed no ^{1}H signals at frequencies above 7 ppm, instead ascribing signals at 0.5–2.0 and 3.6 ppm to –OH terminations on the basis of DFT calculations and the assignment of a Ti_2CT_x ^{1}H spectrum in a separate report by Sugahara[68]. These differences may be due to sample preparation, however, we note that the studies of Kobayashi et al. and Sugahara et al. do not provide direct evidence for their terminal –OH assignments (c.f. the ^{1}H–^{13}C HETCOR employed for V_2CT_x and Ti_3CT_x,[35,36] and the ^{1}H{^{93}Nb} TRAPDOR used here). Furthermore, (i) Sugahara et al. found an estimated composition of $Ti_2C(OH)_{0.3}O_{0.7}F_{0.6}Cl_{0.4}$ with a similar etching procedure to Kobayashi et al. (LiF, HCl)[68] and (ii) $Ti_3C_2T_x$ is electronically conducting (so much so that the sample in the Kobayashi et al. study was diluted by a factor of 20 to perform magic angle spinning) but the DFT calculations for –OH shifts include neither –F termination nor Knight shift contributions, which are expected to substantially affect the ^{1}H shifts.[38] It is possible that due to the high conductivity of their samples, Kobayashi et al. and Sugahara et al. are not able to observe the –OH terminations due to rf penetration or bulk magnetic susceptibility broadening effects.

The –OH ^{1}H shifts for the Nb MXenes are similar to those observed for $Ti_3C_2T_x$ by Hope et al.[36] and Anayee et al.[37], although as the 26 ppm signal for Nb_2CT_x is outside the diamagnetic range for ^{1}H NMR, there must also be at least a small Knight shift, as for V_2CT_x. The –F terminations, on the other hand, are observed at higher frequencies for the Nb MXenes than for V_2CT_x and $Ti_3C_2T_x$, which could be due to more covalent Nb–F bonding caused by the more diffuse $4d$ orbitals. In general, the multiple NMR signals observed for –OH and –F terminations, and the dependence on the synthesis, can be ascribed to distinct local environments due to different arrangements of the surface terminations (–OH, –O, –F and

termination vacancy), as well as interlayer H_2O, as shown, for instance, for the –F terminations in $Nb_4C_3T_x$.

Table 3 – Summary of the chemical shifts of ^{1}H and ^{19}F surface species observed for different MXenes.

Phase	Source	δ [1]H /ppm	δ [19]F /ppm
Nb_2CT_x	This work	12.2, 19.5, 26.0	−20, −132
$Nb_4C_3T_x$	This work	15.0	−80, −190
V_2CT_x	Harris et al.[35]	27, 85	−265
$Ti_3C_2T_x$	Hope et al.[36]	12.5/18.6[a]	−227/−255[a]
	Anayee et al.[37]	15/20[a]	Not attempted
	Kobayashi et al.[38]	0.5–2.0, 3.6	"Unable to observe"[38]

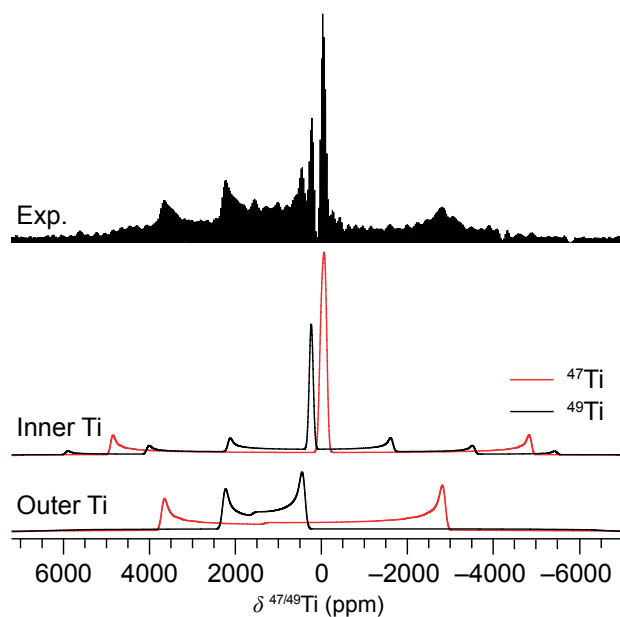[a]Depending on the synthesis procedure

Figure 10 – [47/49]Ti static QCPMG spectrum of Ti_3AlC_2 acquired at 16.4 T by taking the skyline projection of five VOCS sub-spectra. The simulated quadrupolar [47]Ti and [49]Ti patterns for the inner and outer Ti sites are shown below the experimental spectrum. Simulation parameters are given in Table 4.

Extending the transition-metal NMR of MAX phases. Based on insights gained from the [93]Nb NMR of Nb MAX phases, we were also able to interpret the [47/49]Ti NMR of Ti_3AlC_2, another technologically important MAX phase used as a high temperature ceramic, and the precursor to the most studied MXene phase, $Ti_3C_2T_x$.[69,5,7] Ti NMR is particularly challenging to interpret because its two NMR-active isotopes, [47]Ti and [49]Ti, are both quadrupolar (I = 5/2 and 7/2, respectively) and by chance have extremely similar gyromagnetic ratios, differing by only 267 ppm (0.027%). As a result, overlapping quadrupolar lineshapes for both isotopes are typically observed in a single spectrum.[46,70,71] Nevertheless, the [47]Ti and [49]Ti signals of both the inner

and outer Ti environments in Ti_3AlC_2 could be assigned from the overlapped spectrum (Figure 10) by considering that the C_Q values for the outer/inner metal sites are expected to differ by an order-of-magnitude (c.f. ^{93}Nb in Nb_4AlC_3), and by using the fixed relationships between the nuclear properties of $^{47/49}$Ti. The quadrupolar parameters of the two titanium sites for both nuclei are given in Table 4: since the frequency separation and ratio of the quadrupolar coupling constants for the ^{47}Ti and ^{49}Ti signals are fixed by their respective nuclear properties, there are fewer independent parameters than it might seem, and the simultaneous agreement of both signals with the measured spectrum affords a high confidence in the NMR parameters. As also observed for the Nb MAX phases (Table 2), the Ti sites exhibit axial quadrupolar tensors, consistent with the crystallographic symmetry, while the inner site has a modest C_Q relative to the outer site.

Table 4 – Fitted ^{47}Ti and ^{49}Ti quadrupolar parameters for the two crystallographic Ti sites in Ti_3AlC_2 extracted from Figure 10. The estimated errors in the last digit are given in parentheses. Note that the simulated spectra were insensitive to the CSA parameters, which were therefore not determined.

Site	Nucleus	δ_{iso} (ppm)[a]	C_Q (MHz)	η_Q
Inner	^{47}Ti	−27(10)	2.57[b]	0.00[c]
	^{49}Ti	239(10)	2.10[b]	0.00[c]
Outer	^{47}Ti	1338(20)	18.1(3)	0.00(5)
	^{49}Ti	1604(20)	14.8(2)	0.00(5)

[a]The ^{47}Ti shifts are referenced to ^{49}Ti and as such are 266 ppm less than the corresponding ^{49}Ti shift, rather than equal.
[b]This represents an upper bound, based on the linewidth of the ^{47}Ti signal.
[c]The inherent linewidth is too broad to determine η from the lineshape of the central transition, and the turning points of the satellite transitions cannot be identified, however $\eta = 0$ is consistent with the crystallographic symmetry.

Conclusions

An extensive survey of the NMR properties of the Nb MAX and MXene phases has been presented. The multinuclear approach adopted in this study provides complementary measurements of the local structural and electronic properties of the MAX and MXene phases, identifies the nature and connectivity of MXene surface terminating species, and enables unambiguous detection of a number of impurity phases.

^{27}Al and ^{93}Nb NMR spectra of the MAX phases Nb$_2$AlC and Nb$_4$AlC$_3$ have been recorded under static and MAS conditions with high resolution and wideline techniques, allowing extraction of the full anisotropic shift and quadrupolar tensors. The insights gained from the Nb MAX phases also then enabled the interpretation of the $^{47/49}$Ti spectrum of Ti$_3$AlC$_2$. The quadrupolar parameters extracted from the spectra were in close agreement with DFT calculations, affording a detailed view of the local coordination environments. The ^{27}Al, ^{93}Nb and ^{13}C spectra also reveal impurity phases in both Nb$_2$AlC and Nb$_4$AlC$_3$, including aluminium oxide, hydrated aluminium fluoride, aluminium carbide/oxycarbide/nitride, niobium metal, and (possibly nonstoichiometric) NbC$_x$ species. Many of these impurities are not apparent from diffraction alone and these results should serve as a guide for future synthesis efforts.

Following the etching process, the conversion to form MXenes was confirmed by ^{13}C NMR, although the presence of unreacted Nb$_2$AlC is apparent in the ^{93}Nb, ^{27}Al, and ^{13}C spectra of the Nb$_2$CT$_x$ sample. ^{93}Nb environments become notably more asymmetric in the MXenes, demonstrating the reduction of symmetry at the surface. The quadrupolar coupling is still lower than calculated for a bare surface, however, pointing to the presence of surface terminations; these surface terminations are key in determining the performance of MXenes in various applications. –OH and –F terminations have been identified for both Nb$_2$CT$_x$ and Nb$_4$C$_3$T$_x$ in the ^{1}H and ^{19}F NMR spectra, their proximity to the surface demonstrated with ^{93}Nb TRAPDOR experiments, and a comparison made with previous studies on Ti$_3$C$_2$T$_x$ and V$_2$CT$_x$ MXenes. The atomic-scale intermixing of –OH and –F terminations for Nb$_4$C$_3$T$_x$ is seen in the ^{1}H/^{19}F HETCOR spectra, which would be challenging to identify by other techniques, and the different ^{19}F termination environments observed for both MXenes are correlated with the degree of hydrogen bonding to interlayer H$_2$O.

The structural insights derived here should serve as a basis to improve synthetic methods and to guide more in-depth computational modelling, both for the Nb MAX and MXene phases, as well as to facilitate comparisons with the wider family of materials. The nature of the surface terminations and interlayer water in MXenes are key to understanding the functional properties, while further insight into the electronic structure in the MAX phases is of fundamental interest. In this way, structure–property relationships can be developed and both MAX and MXene materials can be optimized for advanced functional applications.

Associated Content

Supplementary information file containing diffraction data; additional NMR spectra of Nb_4AlC_3, Nb_2AlC, $Nb_4C_3T_x$, Nb_2CT_x, Nb_2SnC, and NbC; tables of ^{93}Nb quadrupolar parameters for bare and terminated Nb MXene surfaces.

Author Information

Corresponding Author

Email: cpg27@cam.ac.uk

Notes

The authors declare no competing financial interest.

Acknowledgements

References

(1)   Sun, Z. M. Progress in Research and Development on MAX Phases: A Family of Layered Ternary Compounds. *Int. Mater. Rev.* **2011**, *56* (3), 143–166. https://doi.org/10.1179/1743280410Y.0000000001.

(2)   Barsoum, M. W. The $M_{N+1}AX_N$ Phases: A New Class of Solids; Thermodynamically Stable Nanolaminates. *Prog. Solid State Chem.* **2000**, *28* (1–4), 201–281. https://doi.org/10.1016/S0079-6786(00)00006-6.

(3)   Barsoum, M. W.; Radovic, M. Elastic and Mechanical Properties of the MAX Phases. *Annu. Rev. Mater. Res.* **2011**, *41* (1), 195–227. https://doi.org/10.1146/annurev-matsci-062910-100448.

(4)   Barsoum, M. W.; Eklund, P. The $M_{n+1}AX_n$ Phases: The Precursors for MXenes. In *2D Metal Carbides and Nitrides (MXenes)*; Anasori, B., Gogotsi, Y., Eds.; Springer International Publishing: Cham, 2019; pp 15–35. https://doi.org/10.1007/978-3-030-19026-2_2.

(5)   Naguib, M.; Kurtoglu, M.; Presser, V.; Lu, J.; Niu, J.; Heon, M.; Hultman, L.; Gogotsi, Y.; Barsoum, M. W. Two-Dimensional Nanocrystals Produced by Exfoliation of Ti_3AlC_2. *Adv. Mater.* **2011**, *23* (37), 4248–4253. https://doi.org/10.1002/adma.201102306.

(6)   Radovic, M.; Barsoum, M. W. MAX Phases: Bridging the Gap between Metals and Ceramics. *Am. Ceram. Soc. Bull.* **2013**, *92* (3), 20–27.

(7)   Anasori, B.; Lukatskaya, M. R.; Gogotsi, Y. 2D Metal Carbides and Nitrides (MXenes) for Energy Storage. *Nat. Rev. Mater.* **2017**, *2*, 16098. https://doi.org/10.1038/natrevmats.2016.98.

(8)   Li, N.; Li, Y.; Zhu, X.; Huang, C.; Kai, J.-J.; Fan, J. Theoretical Investigation of the Structure–Property Correlation of MXenes as Anode Materials for Alkali Metal Ion Batteries. *J. Phys. Chem. C* **2020**, *124* (28), 14978–14986. https://doi.org/10.1021/acs.jpcc.0c02968.

(9)   Gao, G.; O'Mullane, A. P.; Du, A. 2D MXenes: A New Family of Promising Catalysts for the Hydrogen Evolution Reaction. *ACS Catal.* **2017**, *7* (1), 494–500. https://doi.org/10.1021/acscatal.6b02754.

(10)   Su, T.; Peng, R.; Hood, Z. D.; Naguib, M.; Ivanov, I. N.; Keum, J. K.; Qin, Z.; Guo, Z.; Wu, Z. One-Step Synthesis of Nb_2O_5/C/Nb_2C (MXene) Composites and Their Use as Photocatalysts for Hydrogen Evolution. *ChemSusChem* **2018**, *11* (4), 688–699. https://doi.org/10.1002/cssc.201702317.

(11) Ma, T. Y.; Cao, J. L.; Jaroniec, M.; Qiao, S. Z. Interacting Carbon Nitride and Titanium Carbide Nanosheets for High-Performance Oxygen Evolution. *Angew. Chem. Int. Ed.* **2016**, *55* (3), 1138–1142. https://doi.org/10.1002/anie.201509758.

(12) Xie, X.; Chen, S.; Ding, W.; Nie, Y.; Wei, Z. An Extraordinarily Stable Catalyst: Pt NPs Supported on Two-Dimensional $Ti_3C_2X_2$ (X = OH, F) Nanosheets for Oxygen Reduction Reaction. *Chem. Commun.* **2013**, *49* (86), 10112. https://doi.org/10.1039/c3cc44428g.

(13) Lin, H.; Gao, S.; Dai, C.; Chen, Y.; Shi, J. A Two-Dimensional Biodegradable Niobium Carbide (MXene) for Photothermal Tumor Eradication in NIR-I and NIR-II Biowindows. *J. Am. Chem. Soc.* **2017**, *139* (45), 16235–16247. https://doi.org/10.1021/jacs.7b07818.

(14) Shahzad, F.; Alhabeb, M.; Hatter, C. B.; Anasori, B.; Man Hong, S.; Koo, C. M.; Gogotsi, Y. Electromagnetic Interference Shielding with 2D Transition Metal Carbides (MXenes). *Science* **2016**, *353* (6304), 1137–1140. https://doi.org/10.1126/science.aag2421.

(15) Song, S.; Liu, J.; Zhou, C.; Jia, Q.; Luo, H.; Deng, L.; Wang, X. Nb_2O_5/Nb_2CT_x Composites with Different Morphologies through Oxidation of Nb_2CT_x MXene for High-Performance Microwave Absorption. *J. Alloys Compd.* **2020**, *843*, 155713. https://doi.org/10.1016/j.jallcom.2020.155713.

(16) Sarycheva, A.; Polemi, A.; Liu, Y.; Dandekar, K.; Anasori, B.; Gogotsi, Y. 2D Titanium Carbide (MXene) for Wireless Communication. *Sci. Adv.* **2018**, *4* (9), eaau0920. https://doi.org/10.1126/sciadv.aau0920.

(17) Xie, Y.; Naguib, M.; Mochalin, V. N.; Barsoum, M. W.; Gogotsi, Y.; Yu, X.; Nam, K.-W.; Yang, X.-Q.; Kolesnikov, A. I.; Kent, P. R. C. Role of Surface Structure on Li-Ion Energy Storage Capacity of Two-Dimensional Transition-Metal Carbides. *J. Am. Chem. Soc.* **2014**, *136* (17), 6385–6394. https://doi.org/10.1021/ja501520b.

(18) Eames, C.; Islam, M. S. Ion Intercalation into Two-Dimensional Transition-Metal Carbides: Global Screening for New High Capacity Battery Materials. *J. Am. Chem. Soc.* **2014**. https://doi.org/10.1021/ja508154e.

(19) Hart, J. L.; Hantanasirisakul, K.; Lang, A. C.; Anasori, B.; Pinto, D.; Pivak, Y.; van Omme, J. T.; May, S. J.; Gogotsi, Y.; Taheri, M. L. Control of MXenes' Electronic Properties through Termination and Intercalation. *Nat. Commun.* **2019**, *10* (1), 522. https://doi.org/10.1038/s41467-018-08169-8.

(20) Kim, H.; Alshareef, H. N. MXetronics: MXene-Enabled Electronic and Photonic Devices. *ACS Mater. Lett.* **2020**, *2* (1), 55–70. https://doi.org/10.1021/acsmaterialslett.9b00419.

(21) Jeitschko, W.; Nowotny, H.; Benesovsky, F. Kohlenstoffhaltige ternäre Verbindungen (H-Phase). *Monatsh Chem* **1963**, *94*, 672–676.

(22) Jeitschko, W.; Nowotny, H.; Benesovsky, F. Die H-Phasen Ti_2TlC, Ti_2PbC, Nb_2InC, Nb_2SnC und Ta_2GaC. *Monatsh Chem* **1964**, *95*, 431–435.

(23) Hu, C.; Li, F.; Zhang, J.; Wang, J.; Wang, J.; Zhou, Y. Nb_4AlC_3: A New Compound Belonging to the MAX Phases. *Scr. Mater.* **2007**, *57* (10), 893–896. https://doi.org/10.1016/j.scriptamat.2007.07.038.

(24) Naguib, M.; Halim, J.; Lu, J.; Cook, K. M.; Hultman, L.; Gogotsi, Y.; Barsoum, M. W. New Two-Dimensional Niobium and Vanadium Carbides as Promising Materials for Li-Ion Batteries. *J. Am. Chem. Soc.* **2013**, *135* (43), 15966–15969. https://doi.org/10.1021/ja405735d.

(25) Ghidiu, M.; Naguib, M.; Shi, C.; Mashtalir, O.; Pan, L. M.; Zhang, B.; Yang, J.; Gogotsi, Y.; Billinge, S. J. L.; Barsoum, M. W. Synthesis and Characterization of

Two-Dimensional Nb_4C_3 (MXene). *Chem Commun* **2014**, *50* (67), 9517–9520. https://doi.org/10.1039/C4CC03366C.

(26) Bai, Y.; He, X.; Wang, R. Lattice Dynamics of Al-Containing MAX-Phase Carbides: A First-Principle Study. *J. Raman Spectrosc.* **2015**, *46* (9), 784–794. https://doi.org/10.1002/jrs.4720.

(27) Zhang, C.; Beidaghi, M.; Naguib, M.; Lukatskaya, M. R.; Zhao, M.-Q.; Dyatkin, B.; Cook, K. M.; Kim, S. J.; Eng, B.; Xiao, X.; Long, D.; Qiao, W.; Dunn, B.; Gogotsi, Y. Synthesis and Charge Storage Properties of Hierarchical Niobium Pentoxide/Carbon/Niobium Carbide (MXene) Hybrid Materials. *Chem. Mater.* **2016**, *28* (11), 3937–3943. https://doi.org/10.1021/acs.chemmater.6b01244.

(28) Zhao, S.; Meng, X.; Zhu, K.; Du, F.; Chen, G.; Wei, Y.; Gogotsi, Y.; Gao, Y. Li-Ion Uptake and Increase in Interlayer Spacing of Nb_4C_3 MXene. *Energy Storage Mater.* **2017**, *8*, 42–48. https://doi.org/10.1016/j.ensm.2017.03.012.

(29) Zhang, C. (John); Kim, S. J.; Ghidiu, M.; Zhao, M.-Q.; Barsoum, M. W.; Nicolosi, V.; Gogotsi, Y. Layered Orthorhombic $Nb_2O_5@Nb_4C_3T_x$ and $TiO_2@Ti_3C_2T_x$ Hierarchical Composites for High Performance Li-Ion Batteries. *Adv. Funct. Mater.* **2016**, *26* (23), 4143–4151. https://doi.org/10.1002/adfm.201600682.

(30) Lipatov, A.; Alhabeb, M.; Lu, H.; Zhao, S.; Loes, M. J.; Vorobeva, N. S.; Dall'Agnese, Y.; Gao, Y.; Gruverman, A.; Gogotsi, Y.; Sinitskii, A. Electrical and Elastic Properties of Individual Single-Layer $Nb_4C_3T_x$ MXene Flakes. *Adv. Electron. Mater.* **2020**, *6* (4), 1901382. https://doi.org/10.1002/aelm.201901382.

(31) Bortolozo, A. D.; Sant'Anna, O. H.; da Luz, M. S.; dos Santos, C. A. M.; Pereira, A. S.; Trentin, K. S.; Machado, A. J. S. Superconductivity in the Nb_2SnC Compound. *Solid State Commun.* **2006**, *139* (2), 57–59. https://doi.org/10.1016/j.ssc.2006.05.006.

(32) Scabarozi, T. H.; Roche, J.; Rosenfeld, A.; Lim, S. H.; Salamanca-Riba, L.; Yong, G.; Takeuchi, I.; Barsoum, M. W.; Hettinger, J. D.; Lofland, S. E. Synthesis and Characterization of Nb_2AlC Thin Films. *Thin Solid Films* **2009**, *517* (9), 2920–2923. https://doi.org/10.1016/j.tsf.2008.12.047.

(33) Kamysbayev, V.; Filatov, A. S.; Hu, H.; Rui, X.; Lagunas, F.; Wang, D.; Klie, R. F.; Talapin, D. V. Covalent Surface Modifications and Superconductivity of Two-Dimensional Metal Carbide MXenes. *Science* **2020**, eaba8311. https://doi.org/10.1126/science.aba8311.

(34) Lue, C. S.; Lin, J. Y.; Xie, B. X. NMR Study of the Ternary Carbides M_2AlC (M=Ti,V,Cr). *Phys. Rev. B* **2006**, *73* (3), 035125. https://doi.org/10.1103/PhysRevB.73.035125.

(35) Harris, K. J.; Bugnet, M.; Naguib, M.; Barsoum, M. W.; Goward, G. R. Direct Measurement of Surface Termination Groups and Their Connectivity in the 2D MXene V_2CT_x Using NMR Spectroscopy. *J. Phys. Chem. C* **2015**, 13713–13720. https://doi.org/10.1021/acs.jpcc.5b03038.

(36) Hope, M. A.; Forse, A. C.; Griffith, K. J.; Lukatskaya, M. R.; Ghidiu, M.; Gogotsi, Y.; Grey, C. P. NMR Reveals the Surface Functionalisation of Ti_3C_2 MXene. *Phys. Chem. Chem. Phys.* **2016**, *18* (7). https://doi.org/10.1039/c6cp00330c.

(37) Anayee, M.; Kurra, N.; Alhabeb, M.; Seredych, M.; Hedhili, M. N.; Emwas, A.-H.; Alshareef, H. N.; Anasori, B.; Gogotsi, Y. Role of Acid Mixtures Etching on the Surface Chemistry and Sodium Ion Storage in $Ti_3C_2T_x$ MXene. *Chem. Commun.* **2020**, *56* (45), 6090–6093. https://doi.org/10.1039/D0CC01042A.

(38) Kobayashi, T.; Sun, Y.; Prenger, K. E.; Jiang, D.-E.; Naguib, M.; Pruski, M. On the Nature of Terminating Hydroxyl Groups and Intercalating Water in $Ti_3C_2T_x$ MXenes: A Study by ^{1}H Solid-State NMR and DFT Calculations. *J. Phys. Chem. C* **2020**. https://doi.org/10.1021/acs.jpcc.0c04744.

(39) Chien, P.-H.; Griffith, K. J.; Liu, H.; Gan, Z.; Hu, Y.-Y. Recent Advances in Solid-State Nuclear Magnetic Resonance Techniques for Materials Research. *Annu. Rev. Mater. Res.* **2020**, *50* (1), 493–520. https://doi.org/10.1146/annurev-matsci-091019-011049.

(40) Hung, I.; Zhou, L.; Pourpoint, F.; Grey, C. P.; Gan, Z. Isotropic High Field NMR Spectra of Li-Ion Battery Materials with Anisotropy >1 MHz. *J. Am. Chem. Soc.* **2012**, *134* (4), 1898–1901. https://doi.org/10.1021/ja209600m.

(41) Pecher, O.; Halat, D. M.; Lee, J.; Liu, Z.; Griffith, K. J.; Braun, M.; Grey, C. P. Enhanced Efficiency of Solid-State NMR Investigations of Energy Materials Using an External Automatic Tuning/Matching (eATM) Robot. *J. Magn. Reson.* **2017**, *275*, 127–136. https://doi.org/10.1016/j.jmr.2016.12.008.

(42) Lipton, A. S.; Wright, T. A.; Bowman, M. K.; Reger, D. L.; Ellis, P. D. Solid-State ^{67}Zn NMR Spectroscopy in Bioinorganic Chemistry. Spectra of Four- and Six-Coordinate Zinc Pyrazolylborate Complexes Obtained by Management of Proton Relaxation Rates with a Paramagnetic Dopant. *J. Am. Chem. Soc.* **2002**, *124* (20), 5850–5860. https://doi.org/10.1021/ja0127133.

(43) Prasad, S.; Zhao, P.; Huang, J.; Fitzgerald, J. J.; Shore, J. S. Niobium-93 MQMAS NMR Spectroscopic Study of Alkali and Lead Niobates. *Solid State Nucl. Magn. Reson.* **2001**, *19* (1), 45–62. https://doi.org/10.1006/snmr.2000.0022.

(44) Stone, N. J. Table of Nuclear Electric Quadrupole Moments. *At. Data Nucl. Data Tables* **2016**, *111* (Supplement C), 1–28. https://doi.org/10.1016/j.adt.2015.12.002.

(45) Jakobsen, H. J.; Skibsted, J.; Bildsøe, H.; Nielsen, N. Chr. Magic-Angle Spinning NMR Spectra of Satellite Transitions for Quadrupolar Nuclei in Solids. *J. Magn. Reson.* **1989**, *85*, 173–180.

(46) Mackenzie, K. J. D.; Smith, M. E. *Multinuclear Solid-State NMR of Inorganic Materials*; Pergamon Materials Series; Pergamon: London, 2002; Vol. 6.

(47) Myhra, S.; Crossley, J. A. A.; Barsoum, M. W. Crystal-Chemistry of the Ti_3AlC_2 and Ti_4AlN_3 Layered Carbide/Nitride Phases—Characterization by XPS. *J. Phys. Chem. Solids* **2001**, *62* (4), 811–817. https://doi.org/10.1016/S0022-3697(00)00268-7.

(48) Bräuniger, T.; Jansen, M. Solid-State NMR Spectroscopy of Quadrupolar Nuclei in Inorganic Chemistry. *Z. Für Anorg. Allg. Chem.* **2013**, *639* (6), 857–879. https://doi.org/10.1002/zaac.201300102.

(49) Bräuniger, T.; Chandran, C. V.; Wedig, U.; Jansen, M. NMR Chemical Shift and Quadrupolar Interaction Parameters of Carbon-Coordinated ^{27}Al in Aluminium Carbide, Al_4C_3. *Z. Für Anorg. Allg. Chem.* **2011**, *637* (5), 530–535. https://doi.org/10.1002/zaac.201000445.

(50) Marti, R. M.; Sarou-Kanian, V.; Moran, C. M.; Walton, K. S.; Hayes, S. E. NMR Crystallography of Aluminum Carbide: Impurities in the Reagent and Improved ^{27}Al NMR Tensors. *J. Phys. Chem. C* **2020**, *124* (13), 7238–7243. https://doi.org/10.1021/acs.jpcc.9b11579.

(51) Butler, N. D.; Dupree, R.; Lewis, M. H. The Use of Magic-Angle-Spinning NMR in Structural Studies of Si-Al-O-N Phases. *J. Mater. Sci. Lett.* **1984**, *3* (5), 469–470. https://doi.org/10.1007/BF00724394.

(52) Dupree, R.; Lewis, M. H.; Smith, M. E. Structural Characterization of Ceramic Phases with High-Resolution ^{27}Al NMR. *J. Appl. Crystallogr.* **1988**, *21*, 109–116.

(53) Bräuniger, T.; Kempgens, P.; Harris, R. K.; Howes, A. P.; Liddell, K.; Thompson, D. P. A Combined ^{14}N/^{27}Al Nuclear Magnetic Resonance and Powder X-Ray Diffraction Study of Impurity Phases in *β*-Sialon Ceramics. *Solid State Nucl. Magn. Reson.* **2003**, *23* (1–2), 62–76. https://doi.org/10.1016/S0926-2040(02)00016-4.

(54) Cozzan, C.; Griffith, K. J.; Laurita, G.; Hu, J. G.; Grey, C. P.; Seshadri, R. Structural Evolution and Atom Clustering in β-SiAlON: β-Si$_{6-z}$Al$_z$O$_z$N$_{8-z}$. *Inorg. Chem.* **2017**, *56* (4), 2153–2158. https://doi.org/10.1021/acs.inorgchem.6b02780.

(55) Kim, H. S.; Bugli, G.; Djéga-Mariadassou, G. Preparation and Characterization of Niobium Carbide and Carbonitride. *J. Solid State Chem.* **1999**, *142* (1), 100–107. https://doi.org/10.1006/jssc.1998.7993.

(56) Rempel, A. A.; Gusev, A. I.; Belyaev, M. Y. ^{93}Nb NMR Study of an Ordered and a Disordered Non-Stoichiometric Niobium Carbide. *J. Phys. C Solid State Phys.* **1987**, *20* (34), 5655–5666. https://doi.org/10.1088/0022-3719/20/34/005.

(57) Froidevaux, C.; Rossier, D. N.M.R. Investigation of the Atomic and Electronic Structure of Vanadium and Niobium Carbides. *J. Phys. Chem. Solids* **1967**, *28* (7), 1197–1209. https://doi.org/10.1016/0022-3697(67)90063-7.

(58) Sarycheva, A.; Gogotsi, Y. Raman Spectroscopy Analysis of the Structure and Surface Chemistry of Ti$_3$C$_2$T$_x$ MXene. *Chem. Mater.* **2020**, *32* (8), 3480–3488. https://doi.org/10.1021/acs.chemmater.0c00359.

(59) Mashtalir, O.; Lukatskaya, M. R.; Zhao, M.-Q.; Barsoum, M. W.; Gogotsi, Y. Amine-Assisted Delamination of Nb$_2$C MXene for Li-Ion Energy Storage Devices. *Adv. Mater.* **2015**, *27* (23), 3501–3506. https://doi.org/10.1002/adma.201500604.

(60) Cockreham, C. B.; Zhang, X.; Li, H.; Hammond-Pereira, E.; Sun, J.; Saunders, S. R.; Wang, Y.; Xu, H.; Wu, D. Inhibition of AlF$_3\cdot$3H$_2$O Impurity Formation in Ti$_3$C$_2$T$_x$ MXene Synthesis under a Unique CoFx/HCl Etching Environment. *ACS Appl. Energy Mater.* **2019**, *2* (11), 8145–8152. https://doi.org/10.1021/acsaem.9b01618.

(61) Seredych, M.; Shuck, C. E.; Pinto, D.; Alhabeb, M.; Precetti, E.; Deysher, G.; Anasori, B.; Kurra, N.; Gogotsi, Y. High-Temperature Behavior and Surface Chemistry of Carbide MXenes Studied by Thermal Analysis. *Chem. Mater.* **2019**, *31* (9), 3324–3332. https://doi.org/10.1021/acs.chemmater.9b00397.

(62) Grey, C. P.; Vega, A. J. Determination of the Quadrupole Coupling Constant of the Invisible Aluminum Spins in Zeolite HY with ^{1}H/^{27}Al TRAPDOR NMR. *J. Am. Chem. Soc.* **1995**, *117* (31), 8232–8242. https://doi.org/10.1021/ja00136a022.

(63) Persson, I.; Halim, J.; Hansen, T. W.; Wagner, J. B.; Darakchieva, V.; Palisaitis, J.; Rosen, J.; Persson, P. O. Å. How Much Oxygen Can a MXene Surface Take Before It Breaks? *Adv. Funct. Mater.* **2020**, 1909005. https://doi.org/10.1002/adfm.201909005.

(64) König, R.; Scholz, G.; Pawlik, a.; Jager, C.; Van Rossum, B.; Kemnitz, E. Identification of AlF$_x$(OR)$_y$ Species in Strongly Disordered Aluminum Isopropoxide Fluoride Solids: A Field-Dependent MAS NMR Study. *J. Phys. Chem. C* **2009**, *113*, 15576–15585. https://doi.org/10.1021/jp9066795.

(65) Mouras, S.; Hamwi, A.; Djurado, D.; Cousseins, J. C.; Fawal, Z.; Hajji Mohamad, A.; Dupuis, J. ^{19}F NMR Study of Niobium Pentafluoride–Graphite Intercalation Compounds Prepared under Fluorine Atmosphere. *J. Solid State Chem.* **1989**, *83*, 115–120. https://doi.org/10.1016/0022-4596(89)90060-1

(66) Bloch, F.; Siegert, A. Magnetic Resonance for Nonrotating Fields. *Phys. Rev.* **1940**, *57* (6), 522–527. https://doi.org/10.1103/PhysRev.57.522.

(67) Emsley, L.; Bodenhausen, G. Phase Shifts Induced by Transient Bloch–Siegert Effects in NMR. *Chem. Phys. Lett.* **1990**, *168* (3–4), 297–303. https://doi.org/10.1016/0009-2614(90)85614-I.

(68) Sugahara, A.; Ando, Y.; Kajiyama, S.; Yazawa, K.; Gotoh, K.; Otani, M.; Okubo, M.; Yamada, A. Negative Dielectric Constant of Water Confined in Nanosheets. *Nat. Commun.* **2019**, *10* (1), 850. https://doi.org/10.1038/s41467-019-08789-8.

(69) Tzenov, N. V.; Barsoum, M. W. Synthesis and Characterization of Ti_3AlC_2. *J. Am. Ceram. Soc.* **2004**, *83* (4), 825–832. https://doi.org/10.1111/j.1151-2916.2000.tb01281.x.

(70) Lucier, B. E. G.; Huang, Y. Chapter One - Reviewing [47/49]Ti Solid-State NMR Spectroscopy: From Alloys and Simple Compounds to Catalysts and Porous Materials. In *Annual Reports on NMR Spectroscopy*; Webb, G. A., Ed.; Academic Press, 2016; Vol. 88, pp 1–78.

(71) Xu, J.; Lucier, B. E. G.; Lin, Z.; Sutrisno, A.; Terskikh, V. V.; Huang, Y. New Insights into the Short-Range Structures of Microporous Titanosilicates As Revealed by [47/49]Ti, [23]Na, [39]K, and ^{29}Si Solid-State NMR Spectroscopy. *J. Phys. Chem. C* **2014**, *118* (47), 27353–27365. https://doi.org/10.1021/jp5077966.